KAPL-P-000051
(K96060
CONF-9606178--

ANALYSIS OF UNCLAD AND SUB-CLAD SEMI-ELLIPTICAL FLAWS IN PRESSURE VESSEL STEELS

Hugo Irizarry-Quinones, Bruce D. Macdonald, Wallace J. McAfee

June 1996

NOTICE

KAPL ATOMIC POWER LABORATORY SCHENECTADY, NEW YORK 12301

Operated for the U. S. Department of Energy
by KAPL, Inc. a Lockheed Martin company

DISCLAIMER

Hugo Irizarry-Quiñones[1], Bruce D. Macdonald[1], and Wallace J. McAfee[2]

ANALYSIS OF UNCLAD AND SUB-CLAD SEMI-ELLIPTICAL FLAWS IN PRESSURE VESSEL STEELS

REFERENCE: Irizarry-Quiñones, H., Macdonald, B.D., and McAfee, W.J., "**Analysis of Unclad and Sub-clad Semi-Elliptical Flaws in Pressure Vessel Steels**", Fatigue and Fracture Mechanics: 28th Volume, ASTM STP 1321, J.H. Underwood and B.D. Macdonald, M.R. Mitchell, Eds., American Society for Testing and Materials, 1997.

ABSTRACT: This study was conducted to support warm prestressing experiments on unclad and sub-clad flawed beams loaded in pure bending [1]. Two cladding yield strengths were investigated: 0.6 Sy and 0.8 Sy, where Sy is the yield strength of the base metal. Cladding and base metal were assumed to be stress free at the stress relief temperature for the 3D elastic-plastic finite element analysis used to model the experiments. The model results indicated that when cooled from the stress relief temperature, the cladding was put in tension due to its greater coefficient of thermal expansion. When cooled, the cladding exhibited various amounts of tensile yielding. The degree of yielding depended on the amount of cooling and the strength of the cladding relative to that of the base metal. When subjected to tensile bending stress, the sub-clad flaw elastic-plastic stress intensity factor, $K_I(J)$, was at first dominated by crack closing force due to tensile yielding in the cladding. Thus, imposed loads initially caused no increase in $K_I(J)$ near the clad-base interface. However, $K_I(J)$ at the flaw depth was little affected. When the cladding residual stress was overcome, $K_I(J)$ gradually increased until the cladding began to flow. Thereafter, the rate at which $K_I(J)$ increased with load was the same as that of an unclad beam.

A plastic zone corrected K_I approximation for the unclad flaw was found by the superposition of standard Newman and Raju [2] solutions with those due to a cladding crack closure force approximated by the Kaya and Erdogan solution [3]. These elastic estimates of the effect of cladding in reducing the crack driving force were quite in keeping with the 3D elastic-plastic finite element solution for the sub-clad flaw. The results were also compared with the analysis of clad beam experiments by Keeney [4] and the conclusions by Miyazaki, et al. [5]. A number of sub-clad flaw specimens not subjected to warm prestressing were thought to have suffered degraded toughness caused by locally intensified strain ageing embrittlement (LISAE) due to welding over the preexisting flaw.

KEYWORDS: Warm prestress, cladding, semi-elliptical flaws, sub-clad flaws, stress intensity factors, cladding residual stress, LISAE

---

1. Lockheed Martin Corporation, PO Box 1072, Schenectady, NY 12309-1072
2. Oak Ridge National Laboratory, PO Box 2009, Oak Ridge, TN 37831-8056

INTRODUCTION

The purpose of this study is to calculate stress intensity factors (K_I) along the crack front of sub-clad and unclad four-point bend beams to support the interpretation of warm prestress (WPS) experiments. The WPS experiments were performed at Oak Ridge National Laboratory (ORNL) for Lockheed Martin Corporation [1]. The WPS experimental program was designed to study the fracture resistance enhancement at lower temperatures after a flawed component was pre-loaded at a higher temperature [6]. A summary of the WPS experiments, including a specimen sketch, is presented in Appendix A.

This report describes the analyses performed to model the WPS specimens stress relieving process and the test loading: WPS, cool and unload, and reload to fracture. K_I values were obtained using finite element (FE) methods for different clad materials, cooling conditions, and test loads. The K_I values were calculated using both linear-elastic and elastic-plastic fracture mechanics methods. Elastic-plastic fracture mechanics methods were used to model the stress relieving process of the WPS specimens prior to loading.

FINITE ELEMENT MODELING

As explained in Appendix A, the full beam configuration for the unclad WPS test specimens beams was 864 mm long, 102 mm high, and 127 mm wide. The full beam configuration was a composite design in which only the test section was fabricated from pedigreed material. The test section was 76 mm long, 102 mm deep, and 127 mm wide. Blanks for the test sections were taken from an ASTM A508 Class 2 steel pressure vessel cylinder. Reusable extension arms were electron-beam (EB) welded to the ends of the test section to form the full beam configuration.

The WPS specimen was modeled using quarter symmetry. Two finite element models were created using the PATRAN preprocessor [7]. The resulting unclad WPS specimen FE model, shown in Figure 1, was 432 mm long, 102 mm high, and 64 mm wide. The resulting clad WPS specimen FE model, shown in Figure 2, had an additional layer 6 mm thick to simulate the cladding.

The unclad WPS specimen FE model had 626 elements and 3188 nodes. The sub-clad WPS specimen FE model had 922 elements and 4543 nodes. The cladding thickness was 6 mm and was modeled using two planes of elements 3 mm thick each on the top of the unclad model. The modeled flaw was a 2-to-1 semi-elliptical flaw 80 mm long and 21 mm deep. Details of the crack front are shown in Figure 2.

All the elements of the FE model were 20-noded hexahedron three-dimensional solid elements with the exception of the degenerate hexahedron elements along the crack front. All elements used the 2x2x2 Gaussian integration scheme. The finite element mesh along the crack front was created such that elements along the crack front had a $1/\sqrt{r}$ singularity. Preliminary analyses using different flaw sizes revealed that the difference between the K_I values obtained with a flaw 21 mm deep and those obtained using a flaw 19 mm deep was less than five percent for the unclad WPS specimens. Hence, the 21mm selected flaw depth was considered appropriate for this analysis since it would provide reasonable K_I values. The flaw region was modelled using six partitions along the crack front and four $1/\sqrt{r}$ singularity elements (i.e., quarter-point elements) surrounding the crack tip. (A partition is defined as a surface that is topologically normal to the crack front, and containing either corner-nodes or mid-nodes of a crack front element.) A comparison analysis using nine partitions along the crack front and six $1/\sqrt{r}$ singularity elements surrounding the crack tip resulted in less than one percent difference in the K_I values on an unclad WPS FE model.

To enforce the quarter symmetry of the FE model two of the vertical faces had the normal displacements set equal to zero. On the flaw plane, including the cladding but not the crack face region, the global Y displacement was set equal to zero. No displacement boundary conditions were imposed on the crack face. Along the beam's length centerline, the global Z displacement was set equal to zero. These faces are labeled Y=0 and Z=0 in Figure 1. To simulate the four-point beam reaction loads, the FE model was supported across the top edge, 432 mm from the flaw plane, by setting the global X displacement equal to zero. A point load was applied 64 mm from the flaw plane along the bottom of the FE model. Constraint equations were used in the FE analysis program to ensure that the displacements in the global X direction for the nodes along the loading edge were equal to the node displacement where the point load was applied. To simulate the quarter symmetry of the loading the magnitude of the point load was one-quarter of the actual load applied.

MATERIAL PROPERTIES

The base metal on the WPS test block was modeled using A508 Class 2 low alloy steel properties. With one exception, the cladding was modeled using 3-wire 308-309 stainless steel cladding (SS30X) properties. The remaining analysis was performed using Inconel EN82 cladding properties.

ORNL obtained "as-built" material properties at test temperatures (–129°C to 149°C) performing tensile tests on the same source of material used to fabricate the WPS specimens [1]. These material properties are shown in Appendix B. To model the stress relieving process, cladding and base metal material properties at high temperatures (149°C to 621°C) were obtained from a previously established high temperature material properties database [8]. These material properties are also shown in Appendix B. In this analysis the reference temperature (i.e., stress free temperature) was assumed to be 621°C. This provided an estimate of the residual stresses on the cladding which was judged to be reasonable. The kinematic strain hardening plasticity model was selected to represent the base metal and cladding material responses.

The material properties of the high strength A533 steel extension arms were assumed to be elastic and constant for the proposed temperature range. The Modulus of Elasticity used was 210 MPa. Poisson's ratio was 0.3. The thermal expansion coefficient was 8.3×10^{-6} 1/°C.

To assist the model construction, cladding elements were created on the extension arms. But, since there was no cladding on the extension arms of the WPS specimen, the cladding elements over the extension arms were assumed to be linear-elastic and very soft; the Modulus of Elasticity used was 7 kPa. No thermal expansion was allowed for these elements.

METHODOLOGY FOR COMPUTING K_I VALUES

Since the experiments involved loading, unloading, and reloading, J-integral calculations were valid for only the initial WPS loading. Thereafter, due to changes in the ratios of the principal stresses, the correspondence between flow theory and deformation theory became nonexistent, and other approximations were needed to estimate the crack driving force.

An in-house linear-elastic fracture mechanics finite element code, K13D, was used to calculate elastic K_I values along the crack front on the WPS FE model. Elastic K_I values were determined from the elemental gauss point stresses along the crack front [9]. KI, the plane strain plastic zone corrected (PZC) value of the elastic K_I value [10], was calculated using the following equation:

$$KI = K_I \div \left(\sqrt{1 - K_I^2 / \left(6\pi a \cdot S_y^2 \right)} \right) \quad (1)$$

where a is the flaw depth, and Sy is the yield stress at the WPS temperature. The K_I values were then compared to the $K_I(J)$ values obtained using 3D elastic-plastic finite element analysis.

An in-house elastic-plastic fracture mechanics finite element code, VIRTUAL, was used to calculate $K_I(J)$ values along the crack front on the WPS FE model. The VIRTUAL code uses the virtual crack extension method to calculate the energy release rate, G, [11][12] which is equal to J, provided that path independence is demonstrated [13]. The VIRTUAL code uses topological data about the crack front nodes and elements to prepare partitions and paths through which it calculates J. A partition is defined as a surface that is topologically normal to the crack front containing either corner-nodes or mid-nodes of a crack front element. A path is roughly analogous to a J-integral contour around the crack tip. Path independence means that the energy release rate, G, is nearly identical for different paths around the crack tip on a partition. The $K_I(J)$ values are computed from J at each of several partitions along the crack front (i.e., $K_I(J) = \sqrt{E'G}$, where $E' = E/(1-\nu^2)$ for plane strain conditions).

The WPS FE model used for these analyses had 13 partitions (i.e., 6 elements) along the crack front. Seven paths were used for partitions passing through corner-nodes and six paths were used for partitions passing through mid-nodes. VIRTUAL performs a 3D energy release rate calculation in a partition-by-partition fashion, with each partition being treated as a 2D plane.

WPS EXPERIMENTS

Displacement Matching

As shown in Figure 3, the crack mouth opening displacement for the clad and unclad WPS beam experiments matches those obtained from the FE models indicating modeling accuracy. The presence of cladding on the WPS model caused a significant reduction of the crack mouth opening displacements when compared to the unclad model. This comparison of elastic-plastic crack mouth opening displacements suggests the qualitative cladding benefit for flaws on the order of thrice the depth of the cladding thickness.

Unclad Beam Results

WPS loads, minimum loads, and fracture loads for the unclad beam specimens are included in Appendix A, Table A1. A comparison of various estimates of the WPS crack driving force is presented in Table 1. PZC K13D results were up to 10% lower than the $K_I(J)$ calculated by VIRTUAL, the larger difference occurring at the higher WPS loads.

A comparison between the K13D results and Newman-Raju formula [2] at the maximum WPS load showed good agreement. Both the Newman-Raju and K13D K_I values were 112 MPa$\sqrt{m}$ at the deepest point of the crack.

The VIRTUAL results indicated that path independence was obtained for this model. As shown in Figure 4, for a given load step and partition, the energy release rate, G, values are nearly identical for different paths around the crack tip.

Clad Beam Stress Relieving and Cooldown Process

Due to the higher coefficient of linear expansion of the cladding compared to that of the base metal, cooling from stress relief temperature to room temperature caused plastic tensile stresses in the cladding and elastic compressive stresses in the neighboring base

metal. In what follows, this differential contraction and plastic deformation of the cladding is referred to as thermal plasticity.

At room temperature the thermally induced tensile stresses in the cladding were higher in the SS30X cladding model than in the EN82 cladding model. This was due to the larger coefficient of thermal expansion for the SS30X when compared to the EN82. As a result, the SS30X cladding (which has a yield stress of 328 MPa) yielded almost completely due to cooling following stress relief. On the other hand, the EN82 cladding (which has a yield stress of 430 MPa) yielded only near the free surface. As a consequence of the lower yield strength of the SS30X cladding, the elastic compressive stresses in the neighboring base metal were lower than those associated with the EN82 cladding. Hence the expectation was that the fracture loads would be lowest for the unclad beams, somewhat higher for the SS30X clad beams, and highest for the EN82 clad beams.

In Figure 5 comparison is made between the effect of thermal plasticity (TP) at the deepest point or center of the flaw, and the edge of the flaw at the clad-base metal interface. As one might expect, the attendant base metal compression is more significant at the edge of the flaw (x's) than the center (o's). The effect diminishes with increasing load due to more prevalent yielding in the cladding.

Effectiveness of Cladding Regarding Crack Driving Force

Figure 6 shows the $K_I(J)$ at the deepest point of the crack as a function of applied WPS load for a thru-clad (surface) flaw and its Newman-Raju elastic solution, for the SS30X clad beam, and for the EN82 clad beam at 149°C. The results for the surface flaw serve to verify the modeling and to indicate the extent of the influence of plasticity. When subjected to the WPS tensile bending stress, the sub-clad flaw stress intensity factor, $K_I(J)$, was at first dominated by crack closing force due to tensile yielding in the cladding. Upon further loading, the cladding completely yielded in tension and could supply no additional closing force. The cladding ligament causes the initial response to resemble that of a buried defect. The EN82 cladding was of higher strength than the SS30X, and therefore caused the greatest departure from the surface flaw response as yielding in the cladding became more pronounced.

Figure 7 shows the $K_I(J)$ at the deepest point of the crack as a function of applied load for the SS30X clad beam at three different temperatures. These curves show that as temperature decreases and cladding strength increases, the crack driving force is more greatly diminished in a manner similar to that shown in Figure 6.

Next, the responses of the unclad and sub-clad flaws are compared to show how the cladding effect can be modeled with elastic solutions. The effect of cladding on the crack driving force as a function of applied load is quantified in Figure 8 for WPS beams in the test program. The 3D elastic-plastic finite element (3DEPFE) values of $K_I(J)$ at the deepest point versus load for each of the flaws are linear, with the sub-clad flaw behaving like a buried defect as was noted in the discussion of Figure 6. When the cladding has completely yielded, the sub-clad flaw response becomes offset below the unclad flaw response by a constant value. This suggests that if $K_I(J)$ for the unclad flaw is known, using for example the Newman-Raju solution with a plastic zone correction, then $K_I(J)$ for the sub-clad flaw can be obtained by subtracting some crack closure force $K_I(J)$ value due to the presence of the cladding.

Approximations to the cladding crack closure forces were determined from existing elastic solutions. The Kaya-Erdogan [3] solution for an edge crack loaded by opposing forces at its free edge was used to represent the fully plastic cladding crack closure force estimate. The SS30X yield stress was used to calculate the force for this "fully plastic" estimate. The crack depth was set equal to that of the surface elliptical flaw. The fully

yielded cladding result was obtained by subtracting the "fully plastic" Kaya-Erdogan solution at yield load from the plastic zone corrected Newman-Raju solution [2] for the surface flaw. This estimate was discontinued at the "fully plastic" estimate, and an elastic estimate was obtained by extending a straight line from this point to the origin. Figure 9 suggests that the combination of these solutions provides a reasonable estimate of the elastic-plastic sub-clad flaw response.

LOCALLY INTENSIFIED STRAIN AGEING EMBRITTLEMENT

Mylonas and Rockey [14] and others, and most recently Dawes [15] have commented on the occurrence of abnormally low toughness near welded over notches. Apparently the thermal strains associated with welding are amplified by the presence of the notch at temperatures in the strain ageing regime, resulting in degraded toughness. One of the more dramatic examples of this locally intensified strain ageing embrittlement (LISAE) was the 1943 complete amidships fracture of the new tanker SS Schenectady while tied up at the dock at night in calm weather [15]. On a less grand scale, the manufacturing procedure for the sub-clad flaw specimens provided all the key ingredients for LISAE as noted in Appendix A. Figure 10 provides several comparisons between sub-clad and surface flawed beams tested at -129°C without prior WPS indicating degradation of toughness.

The trend lines are those seen in Figure 8 for sub-clad and unclad flawed beams. Perhaps the most clear indication of LISAE is provided by comparing the filled and open circles. The filled circle represents a sub-clad flawed specimen which had the cladding removed prior to testing. The open circles represent surface flaw specimens. The toughness degradation due to welding over the flaw appears to be significant. However, the sparseness of the data for the unclad case precludes their quantitative assessment. The x's represent sub-clad flawed beams with the same nominal flaw size which were expected to carry far more load at failure than their surface flawed counterparts. That was the case in only one instance, and in that case the apparent toughness was still degraded. As noted by Macdonald, et al. [1], the WPS evolution was effective in removing this toughness distinction between the sub-clad and unclad flawed beams.

COMPARISON WITH OTHER INVESTIGATORS

The conclusions reached in this report are in agreement with those presented by Miyazaki, et al. [5]. Although their work was based in terms of the stress triaxiality near the crack tip, they predicted that a clad material with a higher yield stress enhances the fracture toughness of a base material. Similar behavior was observed for the EN82 cladding model when compared to the SS30X cladding model, and for the −129°C SS30X cladding model when compared to the 149°C SS30X cladding model. In both of these cases the applied stress intensity factor is less for a given load, which would translate to an enhancement of the fracture toughness.

The overall behavior of the structure was well modeled and it follows the prediction by Keeney, et al. [16] (i.e., the effect of the clad material on an underclad flaw is to suppress crack opening). This is also supported by similar work performed by Electricité de France and analyzed by Keeney [4]. Although differences in FE models, material properties, and boundary conditions prevent a direct comparison of the data and results, the analysis process used in this report agrees with that presented by Keeney.

Other work dealing with sub-clad flawed beams was also reviewed for their potential applicability to this work. The following references include work of potential impact. Reference 17 included an assessment of cladding effects on finite element cracks due only to a pressurized thermal shock. Although thermal effects were considered in this analysis, they were not the only source of loading. Reference 18 included a 2D analysis used to

determine fracture toughness estimates using the η-factor method. In addition, the Reference 18 FE model was refined enough to provide information about the crack tip stress triaxiality using the J-Q Methodology. Unfortunately the model in this work was intended to generate stress intensity factors only and constraint was not considered. Therefore, direct comparison with Reference 18 is not possible. Finally, Reference 19 included the evaluation of stress intensity factors for semi-elliptical flaws using stress intensity factor influence coefficients. Although a number of models with different geometric ratios were presented, a direct comparison with the FE model used in this work was not possible. The geometric ratios of the FE model used in this work were not explicitly presented in Reference 19.

SUMMARY

Three-dimensional elastic-plastic finite element techniques were applied to detailed linear-elastic and elastic-plastic fracture mechanics of WPS experiments using clad and unclad beams in four-point bending. Comparison of load line displacements show good agreement between the experiments and analyses which indicate the adequacy of the FE models. Comparison of linear-elastic with the Newman-Raju approximation also revealed good agreement. Comparison of plastic zone corrected elastic K_I values to elastic-plastic $K_I(J)$ values also showed the adequacy of the FE model and the computational techniques.

When modeling the stress relieving process, the cooldown to room temperature caused metal contraction which induced tensile stresses on the cladding and compressive stresses on the base metal. Larger cooldowns created larger tensile stresses on the cladding and the compressive stresses along the crack front of the sub-clad flaw. When subjected to tensile bending stress, the sub-clad flaw stress intensity factor, $K_I(J)$, was at first dominated by crack closing force due to tensile yielding in the cladding. Upon further loading, the cladding completely yielded in tension and could supply no additional closing force. The trends of the $K_I(J)$ versus applied load curves were below the unclad $K_I(J)$ curve, with the EN82 cladding curve the lowest of the two. Similarly, the $K_I(J)$ versus load curves followed the expected trend with temperature. Lower temperatures experienced reduced $K_I(J)$ values supporting the influence of increased lower yield strength at lower temperatures.

Elastic estimates of the effect of cladding in reducing the crack driving force were quite in keeping with the 3DEPFE solution for the sub-clad flaw. A number of sub-clad flaw specimens not subjected to WPS were thought to have suffered a degradation in toughness due to locally intensified strain ageing embrittlement (LISAE) caused by welding over a preexisting crack.

ACKNOWLEDGMENTS

The authors wish to acknowledge the following individuals for their assistance with this work: PD Vozzola and WW Wilkening for their input to and review of finite element models and techniques used in this analysis; GT Embley and PD Smith for providing insight into the WPS phenomena; and JW Wuthrich for his help with the details of the WPS Test Program.

REFERENCES

[1] Macdonald, BD, et.al., "Analysis of Warm Prestress Data", 27th National Symposium on Fatigue and Fracture Mechanics, Williamsburg, VA, June 1994.

[2] Newman, JC and Raju, IS, "Analysis of Surface Cracks in Finite Plates Under Tension or Bending Loads", NASA Technical Paper 1578, December 1979.

[3] Kaya and Erdogan, "The Stress Intensity Handbook", Del Research Corporation, 1985, Page 2.25.

[4] Keeney, JA, "Cleavage Fracture Analysis of the French Clad Beam Experiments", ORNL/NRC/LTR-94/254, Oak Ridge National Laboratory, October 1994.

[5] Miyazaki, N., Ikeda, T., and Ochi, K., "Constraint Effects of Clad on Underclad Crack", Fatigue and Fracture Mechanics in Pressure Vessel and Piping, PVP-Vol. 304, ASME, 1995.

[6] Chell, GG, Haigh, JR, and Vitek, V, "A Theory of Warm Prestressing: Experimental Validation and the Implications for Elastic Plastic Failure Criteria", CERL Report No. RD/L/N 63/79, 1979.

[7] PATRAN Version 2.5 and P3 Version 1.4 Users Manual, MacNeal-Schwendler Corporation, PDA Engineering, 1994.

[8] Wilkening, WW and Snow, JL, "Analysis of Welding-Induced Residual Stresses with the ADINA System", Computers and Structures, Vol. 47, No. 4/5, pp 767-786, 1993.

[9] Irwin, GR, "Analysis of Stresses and Strains near the End of a Crack Traversing a Plate", Journal of Applied Mechanics, Vol. 24, 1957, pp. 361-364.

[10] Irwin, GR, "Plastic Zone Near a Crack and Fracture Toughness", Sagamore Research Conference Proceedings, Vol. 4, 1961.

[11] deLorenzi HG, "On the Energy Release Rate and the J-Integral of 3-D Crack Configurations", International Journal of Fracture, Vol. 19, 1982, pp. 183-193.

[12] deLorenzi HG, "Energy Release Rate Calculations by the Finite Element Method", Engineering Fracture Mechanics, Vol. 21, 1985, pp.129-143.

[13] Rice JR, "A Path Independent Integral and the Approximate Analysis of Strain Concentrations by Notches and Cracks", Journal of Applied Mechanics, Vol. 35, 1968, pp. 379-386.

[14] Mylonas,C., and Rockey, KC, Welding Journal, Vol.40, No. 7, Research Supplement, 1961, pp 306s-310s.

[15] Dawes, MG, in Fracture Mechanics, 26th Volume, ASTM STP 1256, American Society for Testing and Materials, 1995.

[16] Keeney, JA, Bass, BR, and Pennell, WE, "Evaluation of the Effects of Irradiated Cladding on the Behavior of Shallow Flaws Subjected to Pressurized Thermal Shock Loading", Transactions of the 11th International Conference on Structural Mechanics in Reactor Technology, Vol. G, 1991, pp. 195-200.

[17] Keeney, JA, Bass, BR, Sievers, J., and Xiaoming, L., "Analysis of a Presurized Thermal Lock Experiment for Assessing Cladding Effects on Finite Element Cracks", Fatigue, Flaw Evaluation and Leak Before Break Assessments, PVP-Vol. 280, ASME, 1994.

[18] Keeney, JA, Bass, BR, and McAfee, WJ, "Fracture Analysis of Full Thickness Clad Beams Specimens", 27th National Symposium on Fatigue and Fracture Mechanics, Williamsburg, VA, June 1994.

[19] Keeney, JA and Bryson, JW, "Stress Intensity Factor Influence Coefficients for Semielliptical Inner Surface Flaws in Clad Presure Vessels", Fracture Mechanics: 26th Volume, ASTM STP 1256, 1995.

FIGURES

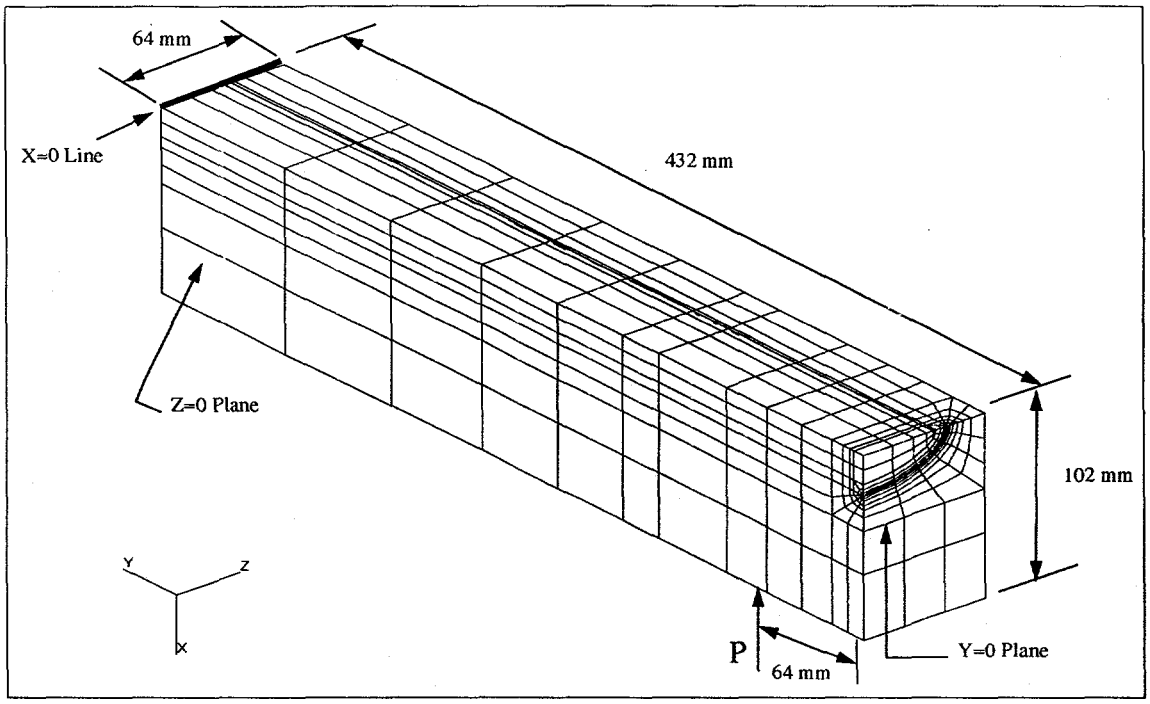

Figure 1. WPS Quarter Symmetry FE Model - Unclad Model

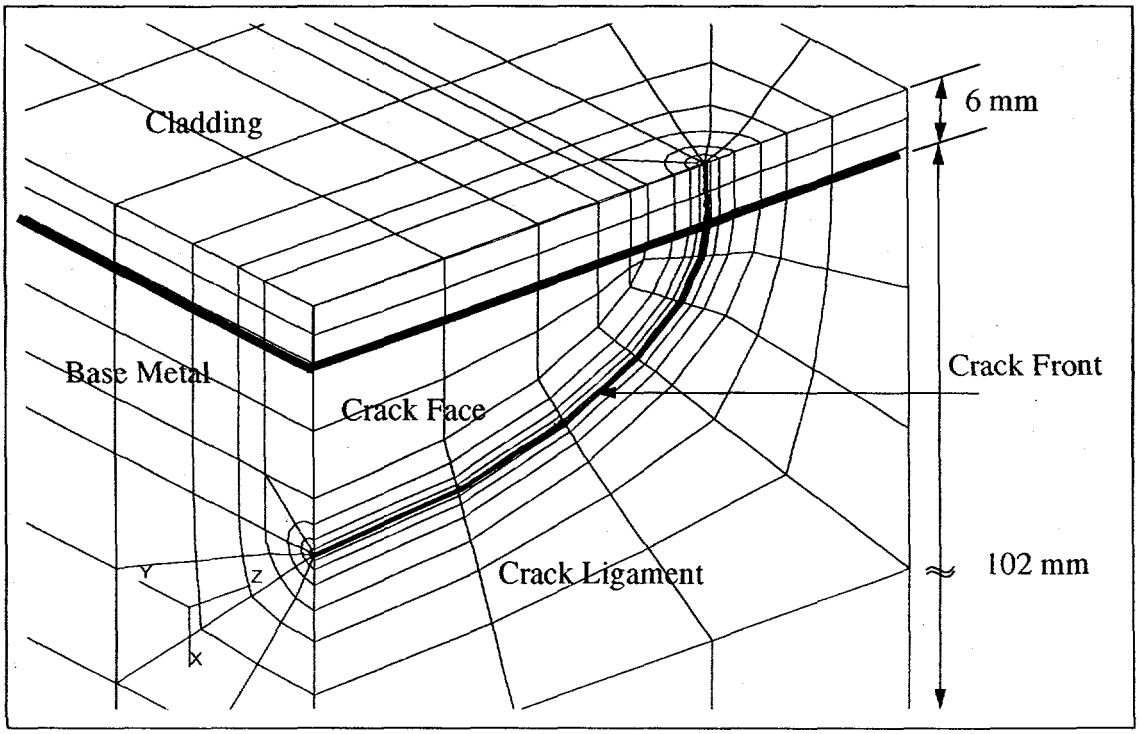

Figure 2. Crack Front Details Quarter Symmetry FE Model - Clad Model

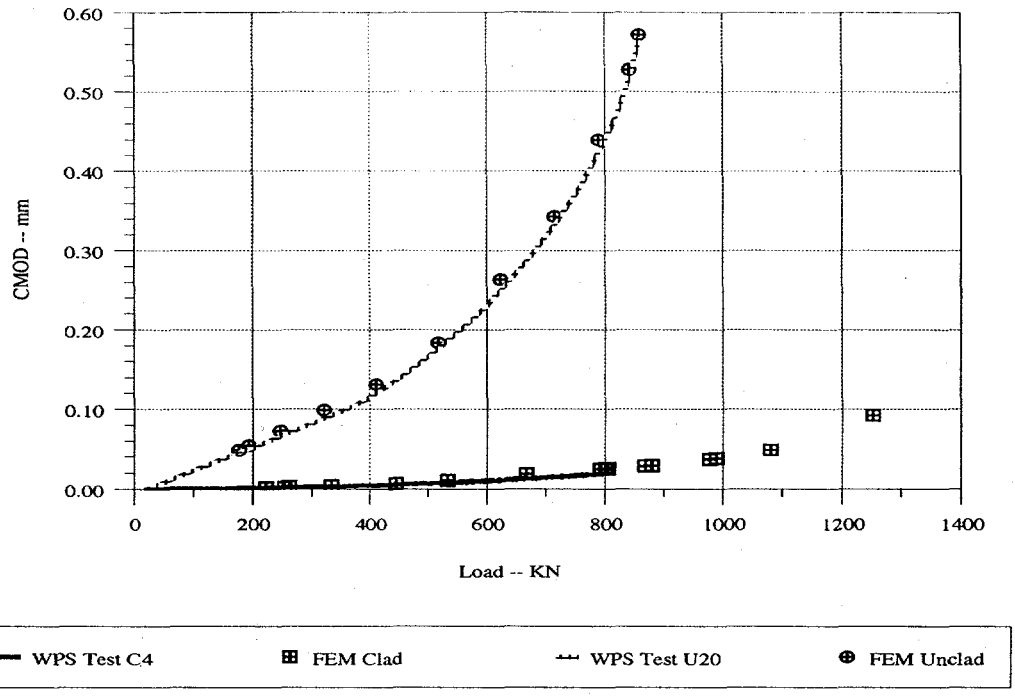

Figure 3. Crack Mouth Opening Displacement for Clad and Unclad Tests and Models (WPS Test C4 = Clad Test; WPS Test U20 = Unclad Test)

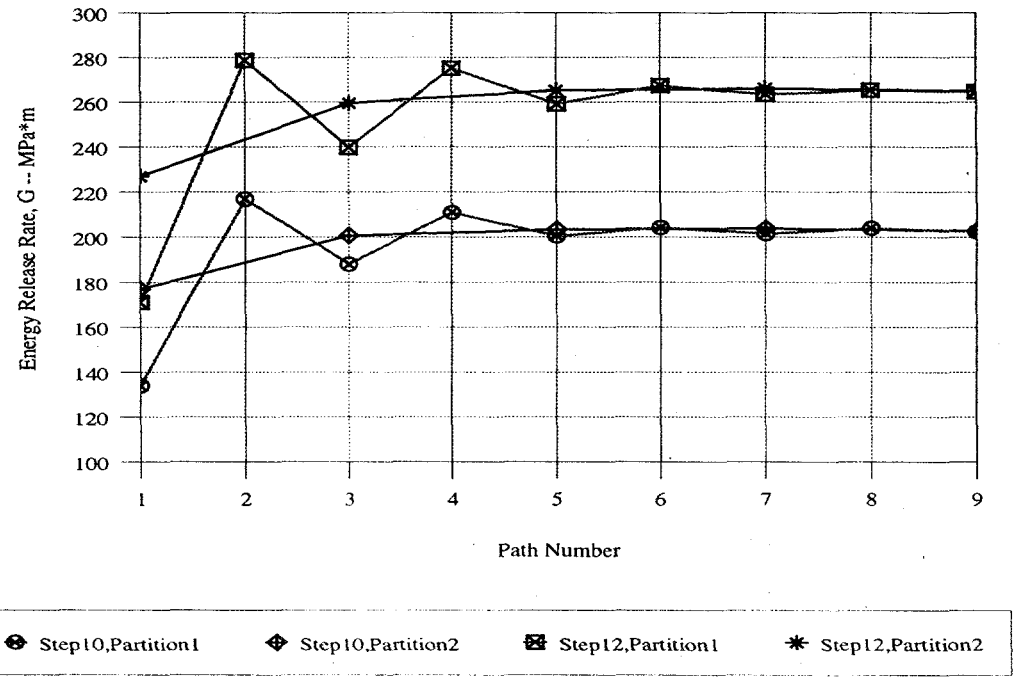

Figure 4. Variation of the Energy Release Rate, G, by Path for Given Partitions (Step 10 and 12 denote increasing load steps used in the FE analysis.)

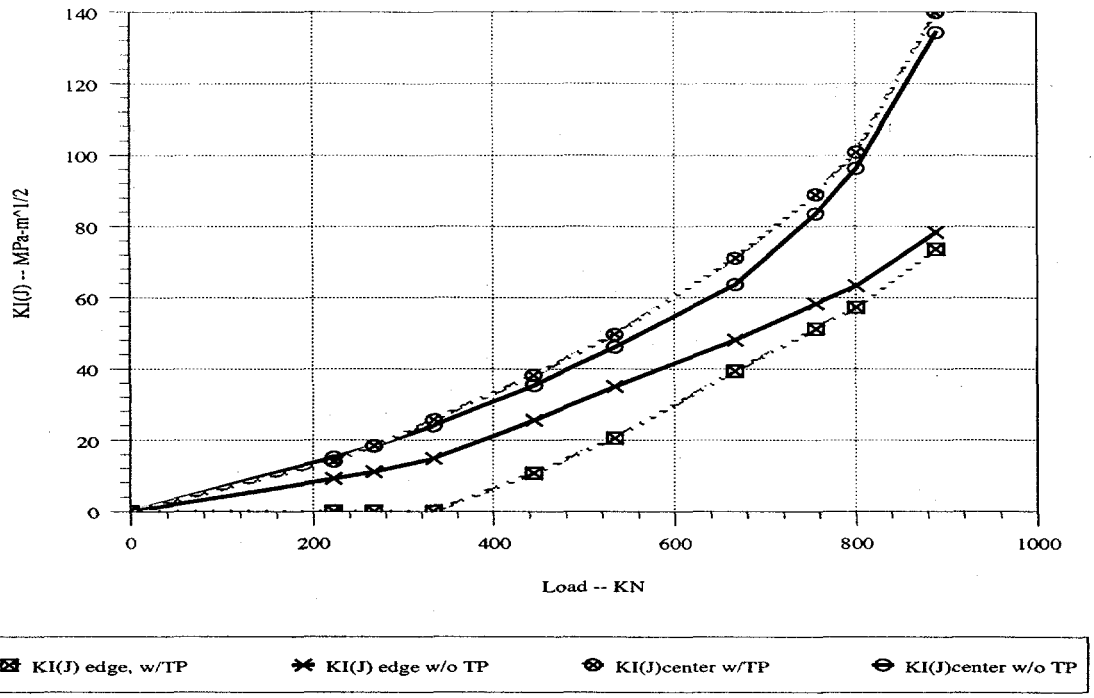

Figure 5. Effect of Cladding Residual Stresses on K(J) for Underclad Cracks During Warm Prestressing (w/ TP = With Thermal Plasticity; w/o TP = Without)

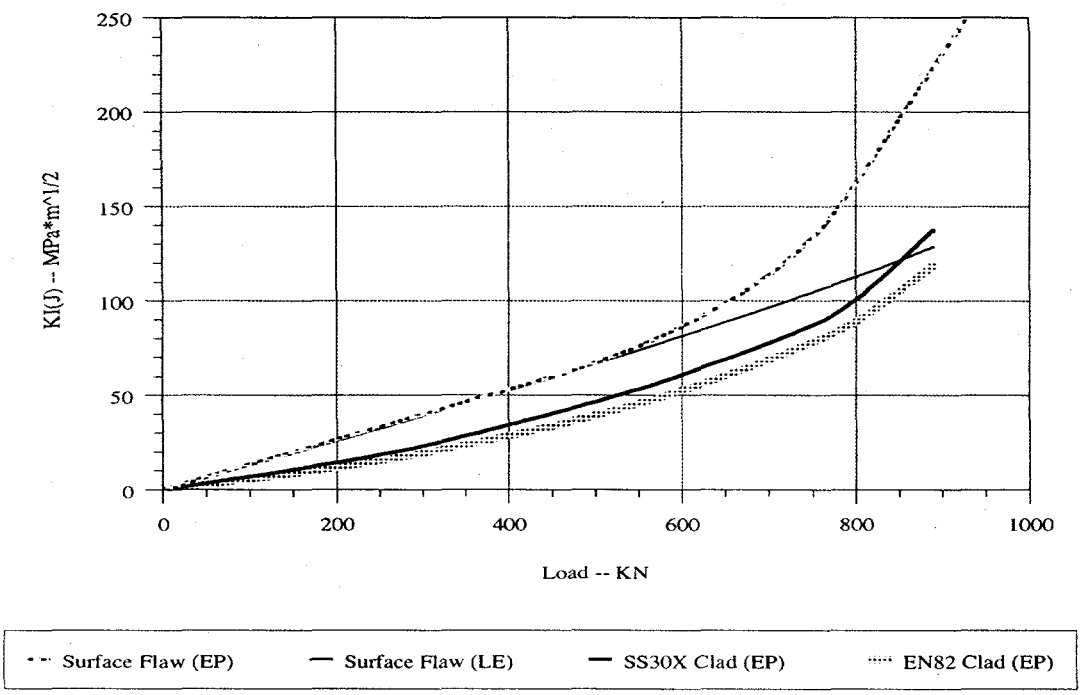

Figure 6. Stress Intensity Factors versus Applied Load for Three Clad Conditions (EP = Elastic-Plastic Analysis; LE = Linear Elastic Analysis)

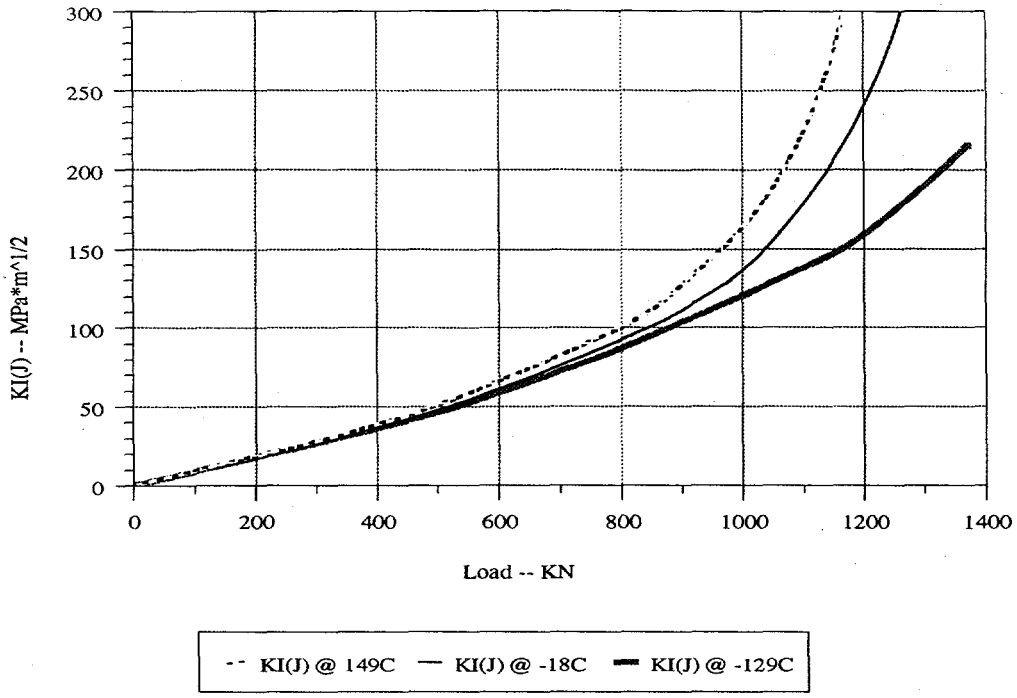

Figure 7. Stress Intensity Factors versus Applied Load for Three Temperatures Using SS30X Clad Model

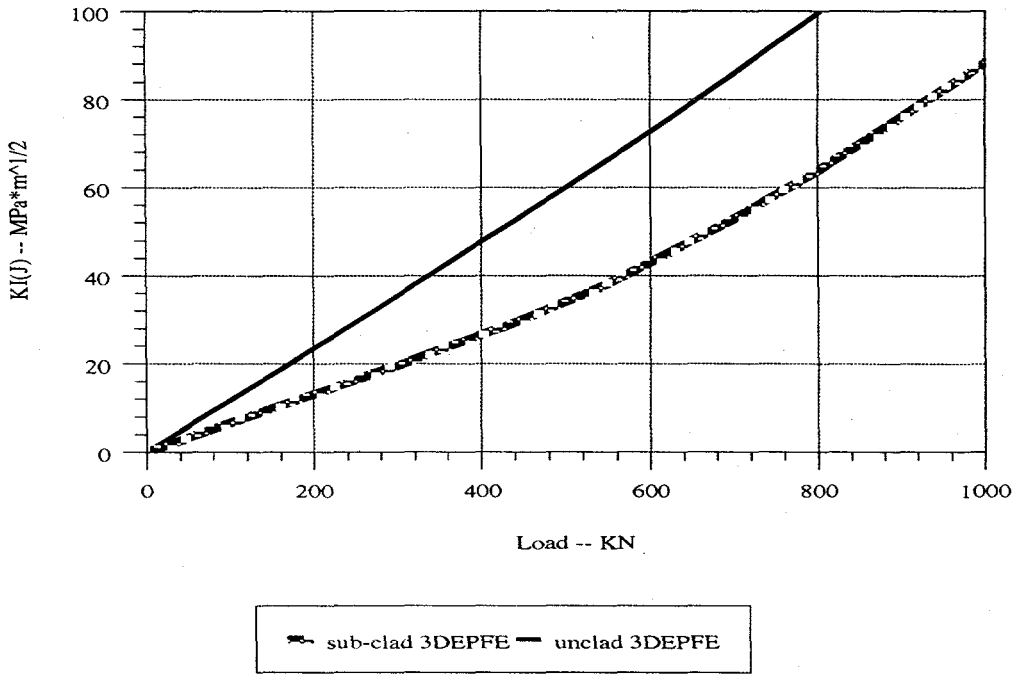

Figure 8. Effect of Cladding on Warm Prestress Beam Crack Driving Force (3DEPFE = 3D Elastic-Plastic Finite Element Analysis)

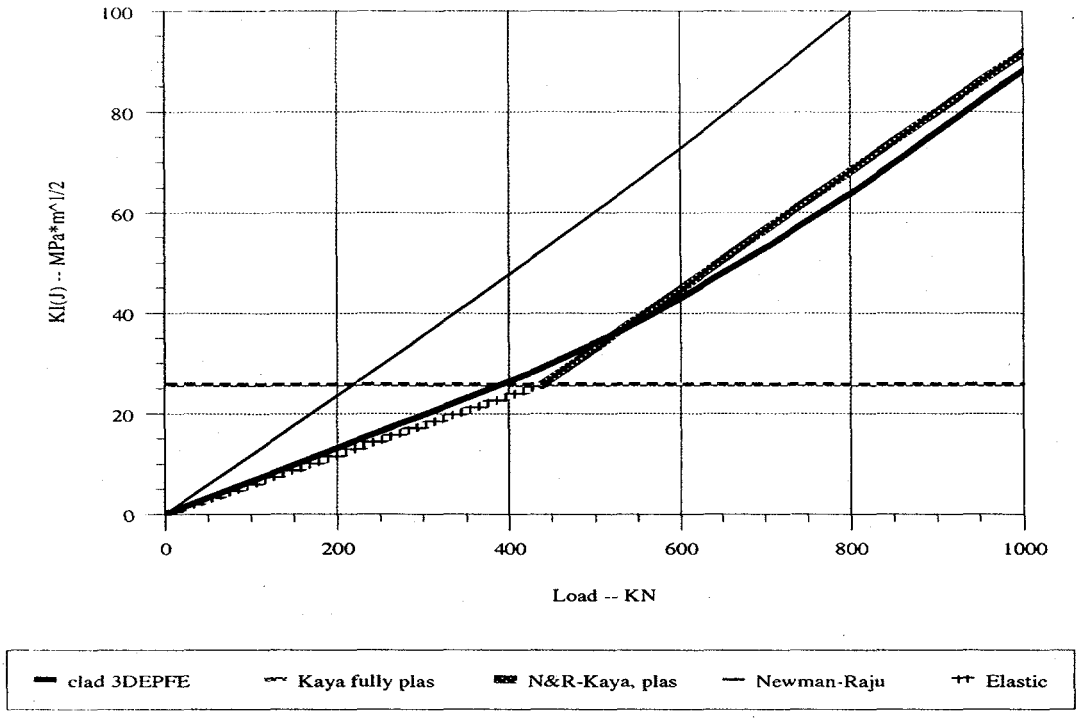

Figure 9. Elastic Estimates of the Effects of Cladding on a Beam Sub-clad Flaw

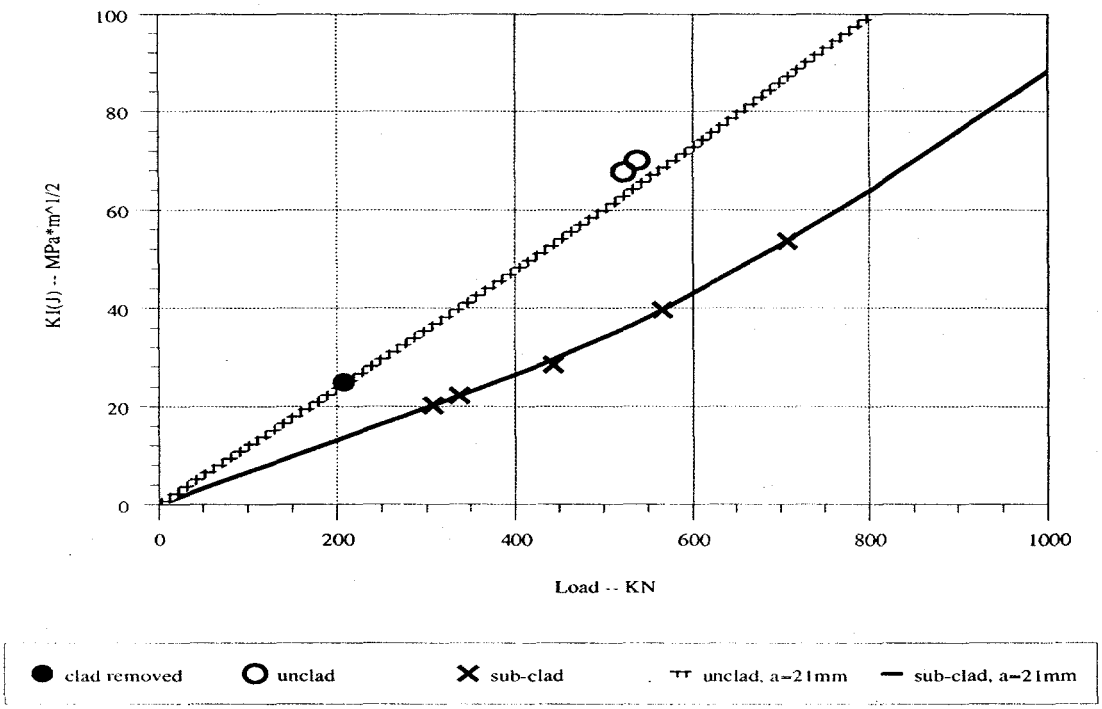

Figure 10. Locally Intensified Strain Aging Embrittlement of Flawed Beams at –129°C

TABLES

Table 1: KI Values for Unclad Beams at WPS Load

Spec. ID	WPS Load		K13D	PZC K13D	Virtual	%Diff
	(Kips)	(KN)	(MPa*m^1/2)	(MPa*m^1/2)	(MPa*m^1/2)	PZC K13D & Virtual
U01	148.9	662	87	90	89	-1.6%
U02	149.3	664	87	90	89	-1.2%
U03	157.0	698	91	95	95	-0.6%
U04	149.1	663	87	90	89	-1.2%
U05	149.5	665	87	90	89	-1.2%
U06	150.4	669	87	91	89	-1.7%
U07	150.2	668	87	91	90	-1.1%
U08	150.4	669	87	91	89	-1.8%
U09	149.7	666	87	91	89	-1.2%
U10	176.1	783	102	108	111	2.9%
U11	175.9	782	102	108	111	2.8%
U12	176.2	784	102	108	111	2.4%
U13	175.1	779	102	108	110	2.5%
U14	176.1	783	102	108	111	2.1%
U15	175.9	782	102	108	111	2.8%
U29	175.8	782	102	108	110	1.7%
U17	176.7	786	103	109	112	3.1%
U18	175.6	781	102	108	111	2.7%
U19	193.3	860	112	120	133	10.6%
U20	193.0	858	112	120	132	10.2%
U28	192.4	856	112	120	132	10.2%
U22	192.6	857	112	120	131	9.8%
U23	193.0	858	112	120	133	10.4%
U24	192.5	856	112	120	132	10.2%
U25	193.1	859	112	120	133	10.5%
U26	193.2	859	112	120	133	10.5%
U27	192.1	854	112	119	130	9.1%

Appendix A

SUMMARY OF WARM PRESTRESSING EXPERIMENTS

Introduction

The unclad warm-prestress (WPS) experimental program consisted of a total of 38 tests in two groups. The first group was a control matrix of 6 specimens tested under isothermal conditions at three different temperatures, −129°C, −73°C, and −18°C. These tests were conducted to provide a baseline for evaluation of the fracture toughness. The second group, the WPS tests, consisted of 32 tests. Three types of WPS load/temperature histories were used. These are shown schematically in Figure A1 and were defined as Load-Unload-Cool-Fracture (LUCF), Load-Cool-Unload-Fracture (LCUF), and Load-Linear Cool and Unload-Fracture (LIN). Data for the unclad WPS tests is shown in Table A1.

The sub-clad WPS experimental program consisted of a total of 8 tests. WPS beams with sub-clad flaws were similarly tested with similar load/temperature histories. The data is shown in Table A2.

Specimen Fabrication

The unclad test specimens were beams 864 mm long, 102 mm high, and 127 mm wide. They were of a composite design in which only the test section was fabricated from pedigreed material. The dimensions and general layout of the test sections are shown in Figure A2. Blanks for the test sections were taken from an ASTM A508 Class 2 steel pressure vessel cylinder.

The unclad blanks were all machined into test sections with final dimensions as shown in Figure A3. The flaw was ram electron discharge machined into the top surface of the test section in the shape of a semi-ellipse 76 mm long and 19 mm deep prior to fatigue pre-cracking. After machining, the test sections were post-weld-heat-treated in Argon at 621°C for 30 hours. This heat treatment was added to simulate the processing environment of the later sub-clad beams. Reusable A533 steel beam extension arms were electron-beam (EB) welded to the ends of the test section to form the full beam configuration. After EB welding the extension arms onto the test section, final machining was performed to remove the EB weld buildup.

The clad specimens were of the same geometry as the unclad with the exception of an additional 6 mm layer of cladding which was deposited after fatigue pre-cracking. The cladding was a either 3-wire 308-309 stainless steel (SS30X) or Inconel EN82 weld deposit.

Instrumentation

Each beam was instrumented to measure crack mouth-opening-displacement (CMOD), surface strain, and temperature. Stroke, or test machine actuator movement, was measured through the test machine controller to obtain an indication of load-line displacement (LLD) for the beam. On the isothermal tests, a linearly variable differential transducer was mounted to measure the LLD directly. However, for the WPS tests, the entire beam was fully enclosed in an environmental chamber, so direct LLD measurements could not be made. The clad beams included additional instrumentation to track cladding deformation.

Temperatures were measured using contact thermocouples (TC). Eight TCs were mounted on the surface of the test section. An additional TC was inserted into the center

of the test section through a side hole. This TC made contact with the material near the center of the block and was used for control of the experiment.

Test Procedure

The procedures contained in ASTM E399 [1] were used as guidelines for these tests, although they do not apply explicitly to the semi-elliptic flaw configuration. After the specimen was instrumented, it was mounted in a four-point bend test fixture, as shown schematically in Figure A2. The specimens were fatigue precracked at room temperature using CMOD change-in-compliance measurements to determine the amount of crack growth. Development tests were performed to establish the final test procedures to yield about 2 mm of crack growth needed to obtain a final flaw about 80 mm long and 21 mm deep. As noted earlier, the 6 mm layer of cladding was deposited after fatigue pre-cracking the clad beams.

After fatigue pre-cracking, in situ instrumentation checks were performed, and the specimen was prepared for the fracture portion of the test. For the control matrix tests, the specimen was cooled to the test temperature and held for a minimum of 20 minutes to establish isothermal conditions in the test section. The specimen was then loaded to failure.

The WPS tests varied from this procedure because of additional equipment requirements. After fatigue pre-cracking, electric heaters were mounted on the specimen, a liquid nitrogen manifold was installed, and an environmental chamber that completely enclosed the specimen was put in place. The specimen was aligned and pre-loaded to 22-kN. Holding the load constant, the specimen was heated to the WPS temperature of 149°C. For a LUCF test, a stable WPS temperature was established and the specified load-unload cycle was applied at a rate of 0.003 Hz using a test machine generated displacement haversine function. Using load-control, the specimen was cooled to the fracture temperature, and the load increased until fracture occurred. For a LCUF test, the specimen was loaded using a load-control ramp function. The load was held constant during cool-down to the fracture temperature. The load was then lowered to the pre-load value, and the load increased until fracture occurred. For the LIN test, the WPS and failure sequences of the test were the same as for the LCUF histogram. However, the LIN test utilized a controller that maintained a linear relationship between the specimen temperature change and the applied load change.

References

[1] 1990 Annual Book of Standards, Volume 03.01, ASTM, 1990.

APPENDIX A FIGURES

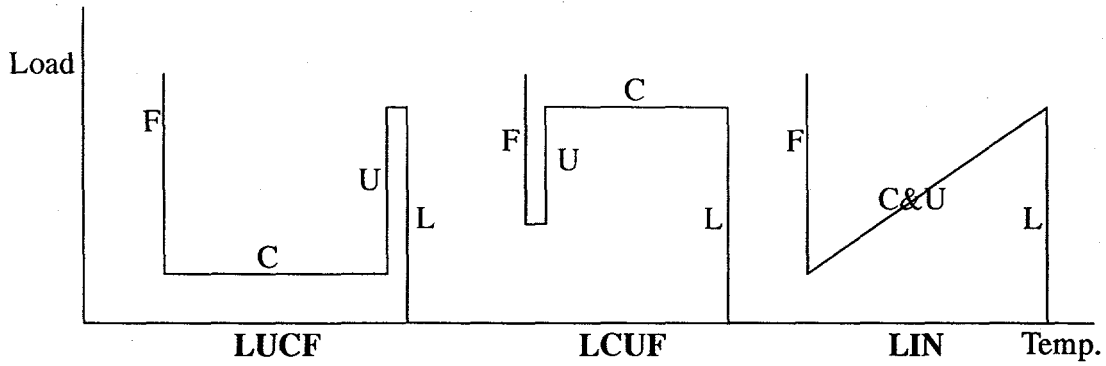

L = Load; U = Unload; C = Cool; F = Fracture

Figure A1. WPS Load/Temperature Schematic

NOT TO SCALE

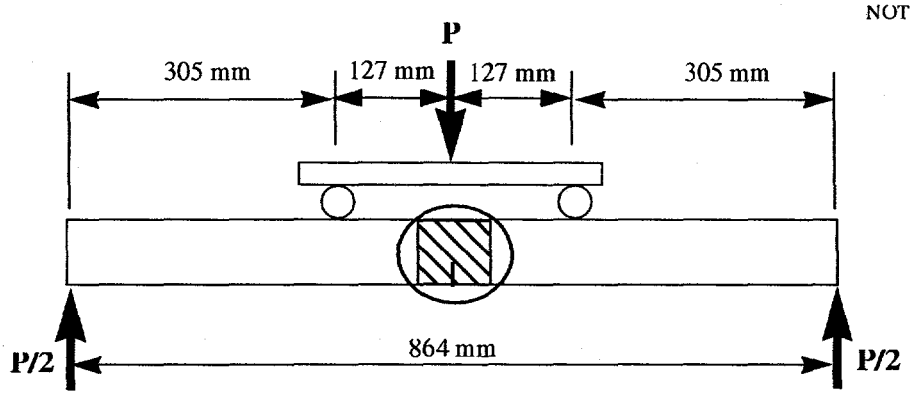

Figure A2. Schematic of WPS Test Beam

NOT TO SCALE

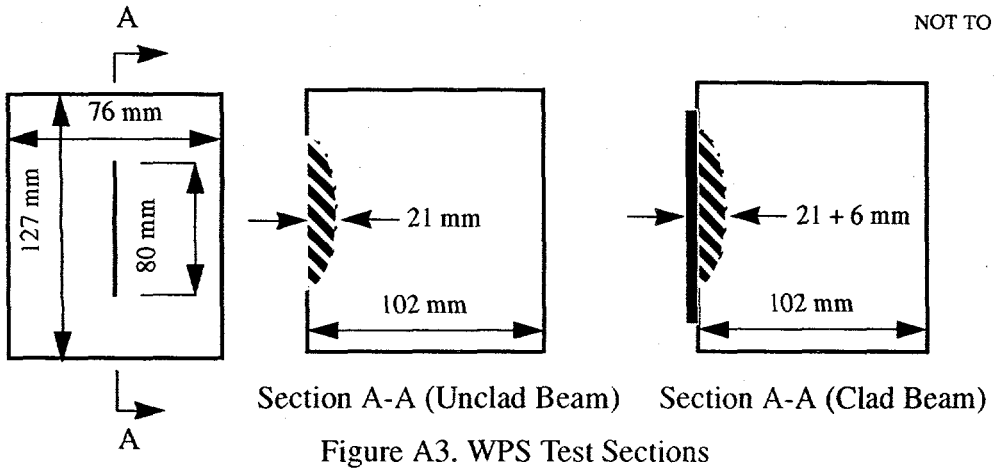

Section A-A (Unclad Beam) Section A-A (Clad Beam)

Figure A3. WPS Test Sections

APPENDIX A TABLES

Table A1: WPS Test Matrix and Results for Unclad Flawed Beams

Specimen	WPS Load (kips)[a]	Minimum Load (kips)[a]	Fracture Temp. (°F)[b]	Fracture Load (kips)[a]
Load - Unload - Cool - Fracture (LUCF)				
U01	148.9	37.5	−200	161.4
U29	175.8	115.4	−200	195.1
U22	192.6	78.7	−200	222.2
U08	150.4	115.9	−100	183.1
U14	176.1	78.3	−100	219.9
U20	193.0	39.7	−100	228.8
U06	150.4	78.5	0	252.8
U12	176.2	40.1	0	236.3
U27	192.1	115.4	0	231.7
Load - Cool - Unload - Fracture (LCUF)				
U07	150.2	115.4	−200	171.9
U13	175.1	79.1	−200	212.3
U19	193.3	38.8	−200	216.8
U05	149.5	77.9	−100	175.2
U11	175.9	39.0	−100	208.8
U26	193.2	114.8	−100	237.5
U03	157.0	39.0	0	224.0
U18	175.6	114.8	0	206.1
U24	192.5	78.4	0	221.5
Load - Linearly Cool and Unload - Fracture (LIN)				
U04	149.1	78.9	−200	172.7
U10	176.1	40.4	−200	161.2
U25	193.1	114.9	−200	231.9
U02	149.3	39.5	−100	200.0
U17	176.7	114.4	−100	207.3
U23	193.0	76.4	−100	217.7
U09	149.7	115.8	0	173.4
U15	175.9	77.5	0	224.7
U28	192.4	37.5	0	217.1

a. 1 kip = 1000 lbf ; 1 lbf = 4.448 N
b. °C = (°F-32)/1.8

Table A2: WPS Test Matrix and Results for Sub-Clad Flawed Beams

Specimen	WPS Load (kips)[a]	Minimum Load (kips)[a]	Fracture Temp. (°F)[b]	Fracture Load (kips)[a]
Load - Unload -Cool - Fracture (LUCF)				
C2	178.0	59.0	0	242.8
C4	180.0	120.0	0	281.4
C1	179.0	58.0	−200	193.3
C3	179.0	120.0	−200	220.6
Load - Cool - Unload - Fracture (LCUF)				
C6	181.0	57.0	0	222.4
C8	181.0	120.0	0	219.8
C5	180.0	60.0	−200	228.4
C7	180.0	120.0	−200	224.6

a. 1 kip = 1000 lbf ; 1 lbf = 4.448 N
b. °C = (°F-32)/1.8

Appendix B

MATERIAL PROPERTIES -- FIGURES AND TABLES

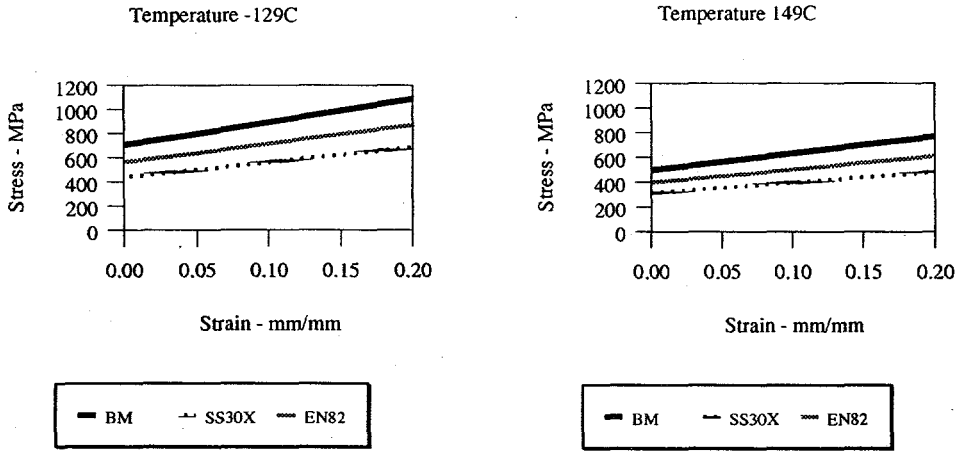

Figure B1. Low Temperature Stress-Strain Curves for Materials Used in Analysis

Table B1: Low Temperature Material Properties used in FE Model [1]

Temp. (C)	SS30X Clad Sy (MPa)	SS30X Clad E (GPa)	SS30X Clad $\alpha_{(mean)}$ (E-06 1/C)	EN82 Clad Sy (MPa)	EN82 Clad E (GPa)	EN82 Clad $\alpha_{(mean)}$ (E-06 1/C)	A508 Cl2 Base Metal Sy (MPa)	A508 Cl2 Base Metal E (GPa)	A508 Cl2 Base Metal $\alpha_{(mean)}$ (E-06 1/C)
-129	391	301	18.05	568	284	14.90	710	351	10.94
-18	363	279	18.62	447	223	15.40	558	276	11.54
149	315	262	19.46	403	201	16.15	503	249	12.44

Table B2: Low Temperature Material Stress-Strain Curves [1]

Temp. (C)	SS30X Clad Stress (MPa)	SS30X Clad Strain (mm/mm)	EN82 Clad Stress (MPa)	EN82 Clad Strain (mm/mm)	A508 Cl2 Base Metal Stress (MPa)	A508 Cl2 Base Metal Strain (mm/mm)
-129	391	0.0013	568	0.0020	710	0.0020
	555	0.040	623	0.040	779	0.040
	8773	2.000	3521	2.000	4402	2.000
-18	363	0.0013	447	0.0020	558	0.0020
	505	0.040	490	0.040	613	0.040
	7842	2.000	2769	2.000	3462	2.000
149	315	0.0012	403	0.0020	503	0.0020
	439	0.040	442	0.040	552	0.040
	6681	2.000	2496	2.000	3120	2.000

Table B3: High Temperature Material Properties used in FE Model [8]

Temp. (C)	SS30X Clad Sy (MPa)	SS30X Clad E (GPa)	SS30X Clad $\alpha_{(mean)}$ (E−6 1/C)	EN82 Clad Sy (MPa)	EN82 Clad E (GPa)	EN82 Clad $\alpha_{(mean)}$ (E−6 1/C)	A508 Cl2 Base Metal Sy (MPa)	A508 Cl2 Base Metal E (GPa)	A508 Cl2 Base Metal $\alpha_{(mean)}$ (E−6 1/C)
260	197	178	20.03	334	174	16.64	382	189	13.05
399	166	167	20.73	320	164	17.27	346	178	13.80
538	135	155	21.44	307	154	17.89	310	167	14.55
677	103	143	22.14	293	145	18.51	274	157	15.31

Table B4: HighTemperature Material Stress-Strain Curves [8]

Temp. (C)	SS30X Clad Stress (Pa)	SS30X Clad Strain (mm/mm)	EN82 Clad Stress (Pa)	EN82 Clad Strain (mm/mm)	A508 Cl2 Base Metal Stress (Pa)	A508 Cl2 Base Metal Strain (mm/mm)
260	1.97E+08	1.10E-03	3.34E+08	1.92E-03	3.82E+08	2.02E-03
	3.00E+08	4.00E-02	4.64E+08	4.00E-02	4.20E+08	4.00E-02
	5.52E+09	2.00E+00	6.57E+09	2.00E+00	2.37E+09	2.00E+00
399	1.66E+08	9.96E-04	3.20E+08	1.95E-03	3.46E+08	1.94E-03
	2.48E+08	4.00E-02	4.35E+08	4.00E-02	3.76E+08	4.00E-02
	4.35E+09	2.00E+00	5.65E+09	2.00E+00	1.90E+09	2.00E+00
538	1.35E+08	8.72E-04	3.07E+08	1.99E-03	3.10E+08	1.85E-03
	1.95E+08	4.00E-02	4.00E+08	4.00E-02	3.32E+08	4.00E-02
	3.19E+09	2.00E+00	4.51E+09	2.00E+00	1.44E+09	2.00E+00
677	1.03E+08	7.27E-04	3.07E+08	2.02E-03	2.74E+08	1.75E-03
	1.42E+08	4.00E-02	2.93E+08	4.00E-02	2.88E+08	4.00E-02
	2.02E+09	2.00E+00	3.36E+09	2.00E+00	9.85E+08	2.00E+00